

APPLICATIONS OF DIGITAL CORE IMAGE ANALYSIS TO THIN-BED EVALUATION

D. T. Georgi and C. Phillips
Core Laboratories, Houston, Tx

R. Hardman
6FF40, Long Beach, Ca

Abstract

Many exploration and exploitation plays involve thinly bedded sequences. These reservoirs frequently test the limits of formation evaluation. Improved reservoir evaluation can be achieved by integrating core photographs with downhole logs. Image analysis of core photographs permits the extraction of quantitative data from the core images that heretofore provided only qualitative information. Recently developed technology makes it possible to quantify sand and shale volumes on a millimeter-by-millimeter basis by using color discrimination. This makes it possible to quantify, as a function of depth, the sand-shale ratio, or, if working with UV fluorescing images, the percent of oil-bearing sand.

Digital image processing can be beneficial in all aspects of formation evaluation. Core images presented on the same scale as log data can be used to calibrate and supplement wireline log data. High resolution wireline logs can be calibrated to predict the presence or absence of sand for net-to-gross determinations on uncored intervals and wells. The conventional log suite can be calibrated to provide an accurate, foot-by-foot sand count. Bed boundary locations derived from core image analysis can be used with forward modeling to evaluate thin-bed log response. Furthermore, the core-derived geometric data can be used to constrain log inversion to obtain better R_t and S_w data.

Introduction

Core-log integration is crucial to formation evaluation and reservoir description. Often core data are only used to provide calibration data for a few matrix parameters in common log analysis equations (e.g., sonic porosity and density porosity). Sometimes special analysis are performed on the core to determine critical exponents for saturation calculations (e.g., formation factor and saturation exponent). And sometimes core data are used to provide data not available from logs (e.g., permeability, capillary pressure, mineralogy). Rarely, however, are the core and log data combined on a foot-by-foot basis to improve reservoir description.

Core images taken with white light, ultraviolet (UV) fluorescent or X-radiography generally are only used to record qualitative information. Typically, core images are used to develop geologic models and to guide the choice of petrophysical models (e.g., homogeneous versus laminated sand models, degree of secondary porosity). However, it is rare that the images are used quantitatively.

Phillips et al. (1991) showed how core images can systematically be quantified and applied to reservoir description. Quantitative image analysis (ImageLog™ analysis) can be used to measure the sand-to-shale ratio (Phillips et al., 1991) and to quantify the sand count millimeter-by-millimeter (Georgi et al., 1991). Such data can further be used to calibrate net sand calculations based on borehole image log data (Phillips et al., 1991). In this paper, we use core image data to

calibrate shale volumes (V_{sh}) calculated from neutron-density cross-plots (Poupon et al., 1970, and Hesslop, 1972). Finally, we combine the core image analysis-derived bed boundaries with induction log forward modeling (Hardman and Shen, 1986) to improve resistivity-based water saturation calculations.

ImageLog Principles

Image analysis is applied routinely to thin sections. However, petrographic image analysis (Gerard et al., 1991) programs are often tied to petrographic microscopes and are not well suited for analysis of core photographs. The system described by Phillips et al. (1991) was specifically designed to handle core photographs and their associated peculiarities (scales, segmented nature, extraneous artifacts, etc.). After the images are captured either directly from core or from the photographs (Fig.1), it is generally necessary to crop unwanted features from the images (e.g., core boxes) and to splice the segmented core photographs into a continuous image that can be further analyzed to produce wireline-like data in log format (Fig. 2).

Once the core photographs are digitized, cropped and possibly enhanced, the interpreter proceeds to "teach" the computer program to differentiate features based on color. To select these features the interpreter highlights (perhaps 60 to 80) representative pixels from the photo set that he wishes to identify (Fig.3a). A three dimensional color histogram is constructed in the red-green-blue color space. Once the histogram is complete, an ellipsoid is used to encapsulate the selected points (Fig. 3b). This ellipsoid is then used to binarize the entire image; pixels whose colors fall within the ellipsoid are assigned a value of 1 (green) and those outside a value of 0 (blue, Fig. 3c). Usually, an ellipsoid works well to encapsulate the selected points; however, other geometric figures are available too (e.g., cubes). It is only necessary to be reasonably consistent in selecting the training points in order to differentiate features based on even the most subtle color changes.

Results from the ImageLog analysis of the core are reported every 120th of a foot and include:

- A Sand-Shale *Ratio* measured along the apparent bed dip,
- A binary *Sand Flag* (1 for sand, 0 for shale) based on the value of the sand-shale ratio. Generally, we use a 0.5 threshold to separate sand from shale.
- A *Thickness Log* in feet (or meters) based on the number of consecutive occurrences of sand intervals (sand flag equal 1). This curve can be used to screen out extremely thin beds.
- A *Percent Log* that summarizes the percent of selected features on a foot-by-foot basis.

The bed boundaries derived from the sand flag, as well as the apparent bed dip angle, can be used as input for induction log forward modeling. Sometimes the sand flag is a better indicator of lithology than the sand-shale ratio because exposure and illumination can vary from photograph to photograph.

It is important to note that the sand-shale ratio makes no assumption about porosity distribution. Effective porosity can be assigned to either the sand or the shale fraction, or distributed among both the sand and the shale. Generally, we assign the effective porosity to the sand fraction. Thus,

$$1 = (V_{ss} + \emptyset) + V_{sh}$$

the selected features (1 or green) represent sand plus porosity. The four items outline above, summary statistics, the number of discrete sand beds, and the overall percent sand in the analyzed interval are tabulated in the ImageLog report.

Application of ImageLog Data to the Quantification of Sand-Shale Ratios in Laminated Sands

In laminated sands, as with other formation types, it is essential to determine both porosity(ϕ) and hydrocarbon saturation for reserve estimates. With care, good porosity estimates can be obtained from core, even in shaly-sands. Although conventional core may be of limited value for direct saturation determinations, core analysis can provide some critical shaly-sand parameters (e.g., CEC). Generally one must rely on saturations derived from wireline log data (most commonly resistivity data). There are several well known equations for interpreting wireline log data in shaly sands (Worthington, 1985). For most of these interpretations it is necessary to compute the volume of shale as well as an effective porosity.

Shale volume estimates are routinely calculated from spontaneous potential, gamma ray and neutron-density porosity logs. Poupon et al. (1970) and Hesslop (1972) construct two pseudo-mineral triangles on a neutron-density crossplot to quantify ϕ , V_{sh} , and V_{clay} . To construct the two triangles (Fig. 4) the interpreter must specify the neutron and density log responses for four points: (1) clean sand or silt, (2) 100% fluid, (3) dry clay, and (4) shale. The clean sand and 100% fluid response are often assigned standard values (e.g., sand: $\phi_N=0\%$, $\phi_D=0\%$; fluid: $\phi_N=100\%$, $\phi_D=100\%$), and the distribution of data on the neutron-density crossplot is used to infer the neutron and density log values associated with the shale point. The wet and dry clay points may be inferred from mineralogical data. However, this can be problematic because the mineralogical data will not include trace elemental data (e.g., B, Gd, Eu) that can significantly alter the neutron log response. The clean sand point can also differ significantly from the nominal value because of the presence of heavy minerals (which increase the matrix density) and thermal neutron absorbers (which increase the apparent neutron porosity). Because of the difficulties associated with assigning representative values to the triangle apexes, these techniques generally require significant local calibration.

In laminated sands, quantification of sand-shale ratios with core image analysis can significantly simplify the calibration of the V_{sh} and V_{ss} (volume of sand) calculations from neutron-density data. The core image data are combined with the neutron-density data. The percent sand derived from the core image data are plotted on the z-axis of a standard neutron-density crossplot, and then the shale and clean sand triangle points are adjusted to agree with the core image results.

Figs. 5 and 6 show the core image data and the neutron and density data for two laminated sand intervals. The sand-shale points were derived from digitized UV fluorescent photographs for these two entirely different areas using ImageLog. The sand fraction data were then used to construct sand-shale porosity triangles (Figs. 7a and 7b). Starting at the 100% fluid point a line is extended through the 100% sand points to zero density porosity (bulk density of 2.65gm/cm^3 , the measured grain density). This line fixes the neutron response for the 100% clean sand point at 12% and -4% for data in Fig. 7a and 7b, respectively. The high apparent neutron porosity for the clean sand point observed in Fig. 7a suggests that either additional borehole corrections are required or that thermal neutron absorbers are present. The location of the 100% shale point is not well determined; however, it must lie on a line parallel to the line connecting the 100% clean sand and the 100% fluid point. In Fig. 7b, the preponderance of data points at 23% density porosity (2.27

gm/cm³) and 42% apparent neutron porosity suggest that these are the appropriate values for the shale point. For the data in Fig. 7a, the shale point lies at 12% density porosity and 48% neutron porosity.

There is good separation on the neutron-density crossplot between the clean sand data and the shaly data points identified with image analysis. However, there is some overlap of intermediate value data points (e.g., 20, 40 and 60%). This non-uniqueness may reflect a non-linear relationship between the degree of shalyness and the visual appearance on the image analysis. Regardless, there is good agreement between the core and the log-crossplot porosity and the computed V_{sh} based on the image analysis calibrated crossplot (Figs. 7a and 7b) and the image analysis results (Figs. 8a and 8b).

Application of ImageLog Data to the Interpretation of Resistivity Data in Laminated Sands

Accounting for the effect of thin, conductive beds is one of the more difficult problems in the interpretation of induction log data. Thin, electrically conductive shale beds can significantly decrease the measured resistivity of hydrocarbon-bearing sands and, therefore give rise to erroneously high water saturations (S_w). Unfortunately, during coring (Rathmell et al., 1990) or core retrieval, hydrocarbons can escape from the core, and, thus, measured saturations may not be representative of the in-situ saturations. Although, some of these problems can be minimized with special coring techniques, cost and operational issues often preclude the use of sponge and or pressure cores. However, conventional core image data (bed geometry) can be used to constrain forward induction log modeling and, thus, enhance resistivity-based water saturation calculations.

The measured induction log response is a function of the formation resistivities, apparent bed dip, and bed geometry. The bed geometry (thickness and location) are uniquely specified by the depths of the bed boundaries. The bed boundary locations and the apparent bed dip angle are derived from the core image data. Unfortunately, the measured apparent resistivities are not a linear function of bed thickness and formation resistivities. Thus, it is not possible to use standard linear deconvolution operators to enhance the vertical resolution of the induction log data, nor is it possible, even in combination with the bed boundary data, to simply invert the measured resistivity to extract the true formation resistivities. However, if we ignore invasion and borehole effects, the core image-derived bed boundaries and an initial "guess" of resistivities can be used with forward modeling to create a synthetic induction log (Hardman and Shen, 1986; Anderson, 1990). An interval-by-interval comparison will then suggest where the initial formation resistivity must be increased or decreased to improve the fit between the measured and computed induction log resistivities. With additional iterations the formation's resistivities can be improved (Wallace et al., 1991) until the computed and measured resistivity logs agree. (Of course, there is no guarantee that the solution is unique.) This process has been automated and coded to run on both personal and mainframe computers (Hardman Assoc., 1992).

The above algorithm can be used to easily determine the true formation resistivities without difficulty if the beds are thicker than the thinnest beds that can be resolved with the induction sonde. For the 6FF40 sonde, the thinnest beds that can be resolved are on the order of 10 feet. Anderson et al. (1990) demonstrated that for a series of thin beds, the induction sonde responds to the average formation conductivity (thickness-weighted average of the individual bed conductivities). The algorithm computes the correct average conductivity. Typically, however, some of the beds will tend towards high conductivity, and others, to compensate, will tend towards zero conductivity (infinite resistivity). Because of this behavior, the algorithm is unstable and fails to converge to a meaningful resistivity profile. Thus, it is necessary to add an additional

constraint to stabilize the algorithm when the model contains beds thinner than the resolving power of the induction sonde.

For the examples presented in this paper, we have constrained the resistivities of the shales and forced the resistivities of all the sands within each zone to be equal:

$$R_t(\text{shales}) = 2.5 \Omega\text{m}$$

$$R_t(\text{sand \# 1}) = R_t(\text{sand \# 2}) = \dots = R_t(\text{sand \# n})$$

The bed boundaries and apparent dips derived from image analysis for the core photos corresponding to the logged interval shown in Fig. 8a were used to compute synthetic resistivity data. Although, it is possible to iterate on both the resistivities of the sands and the shales, we have fixed the resistivities of the shales at $2.5\Omega\text{m}$ and only iterated on the resistivities of the sands. Fig. 9a shows the measured and computed resistivity logs for the initial choice of $30\Omega\text{m}$ sands. Fig. 9b shows the final formation resistivities, as well as the measured and computed induction log resistivities. For the upper most sand (x107-x121 ft), a sand formation resistivity of $14.5\Omega\text{m}$ was used. For the lower sand packages, a $70\Omega\text{m}$ resistivity was used. However, it should be noted that the resistivities of the lower sand beds could be significantly higher (i.e., $200\Omega\text{m}$) and the computed resistivities would not differ significantly from those shown in Fig.9b, because the conductivity signal comes predominantly from the conductive shales. One can only conclude that the resistivities of the sands are at least $70\Omega\text{m}$.

The difference between calculated R_t and the measured deep resistivity is quite important to the determination of reserves. The water saturations computed from the R_t are maximum water saturations, and the estimated hydrocarbon reserves (Fig. 10) are conservative minimums. The gross interval thickness of the formation represented in Fig. 9 is 110ft and average porosity is 7.1%. The average water saturation, computed from the deep induction log resistivities, is 82.7%. The average water saturation decreases to 65% when the R_t from the induction log forward modeling are used. Finally, the reserves¹ based on the image analysis and forward induction log modelling (2.7ft) are double those based on the measured deep resistivities (1.3 ft).

Summary

Core and log data when combined on a foot-by-foot basis improve reservoir description and increase reserves. Core image analysis data facilitated the choice of clean sand and shale points for V_{sh} computations from neutron-density data. Core image analyses were used to provide bed geometry data and induction log forward modelling for improved R_t determination.

¹Hydrocarbon reserves = $\emptyset(\text{net pay})(1-S_w)$.

References

- Anderson, B., Barber, T., Singer, J., and Broussard, T., 1990, ELMOD-Putting Electromagnetic Modeling to Work to Improve Resistivity Log Interpretation., SPWLA 30 Annual Logging Symposium, Paper M, 16 pp.
- Georgi, D. T., Cullen, M. P., Buchanan, T. R., Huber, P. M., and Lyons, S. A. ,1991, Formation Evaluation Contributions to the Cessford Shallow Gas Pilot, Thirteenth Formation Evaluation Symposium, CWLS Paper F, 27pp.
- Gerard, R. E., Philipson, C., A., Manni, F. M., and Marschall, D. M., 1992, "Petrographic Image analysis: An Alternative Method for determining Petrophysical Properties." in I. Palz and S. K. Sengupta (eds.), Automated Pattern Analysis in Petroleum Exploration, p. 249-263.
- Hardman, R. H. and Shen, L.C., 1987, Charts for Correcting Effects of Formation Dip and Hole Deviation on Induction Logs. *Log Analyst* v28, p. 350 - 356.
- Hardman, R. H., and Shen, L. C., 1986, Theory of Induction Sonde in Dipping Beds. *Geophysics* v51, p 800-809.
- Hesslop, A., 1972, Gamma-Ray log response of Shaly Sandstones. *CWLS Symposium*, vol. 5 issue 1, 11pp.
- Phillips, C., DiFoggio, R., and Burleigh, K., 1991, Extracting Information from Digital Images of Core. *Society of Core Analysts, 5th Technical Conference*, Paper SCA-9125. 15 pp.
- Poupon, A. C., Clavier, C., Dumanoir, J., Gaymard, R., and Misk, A., 1970, Log Analysis of Sand Shale Sequences - A Systematic Approach. *J. Pet. Tech.*, p.
- Rathmell, J. J., Tibbits, G. A., Gremley, R.B., Warner, H. R. Jr., and White, E. K., 1990, Development of a Method for Partially Uninvaded Coring in High Permeability Sandstone. *SPE* 20413, p. 89 - 100.
- Wallace, J.P., Osborn, F.F., Shen, L.C., and Lyle, W.D. Jr., 1991, Computer-Aided Interpretation of Induction Logs. *SPWLA 32 Annual Logging Symposium*, Paper X, 16pp.
- Worthington, P. 1985, The Evolution of Shaly-Sand Concepts in Reservoir Evaluation. *Log Analyst*, v26, p. 23- 40.

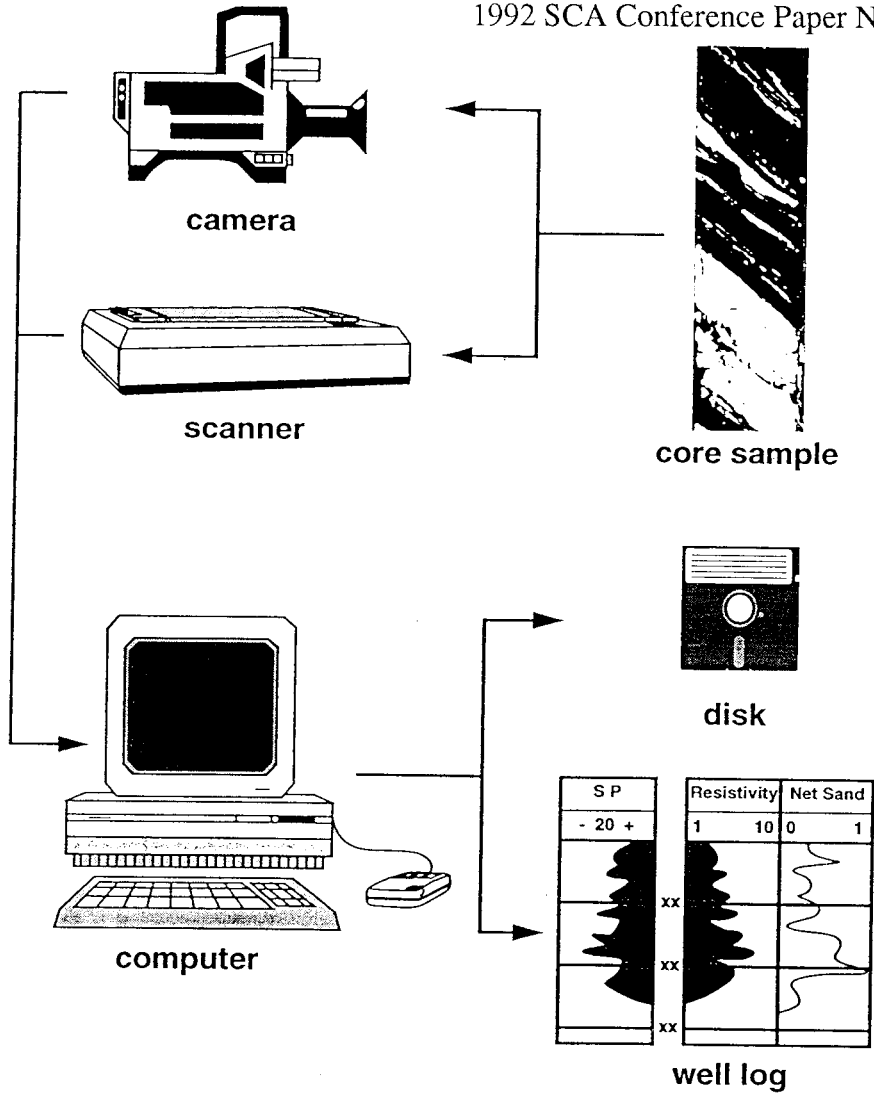


Figure 1. Core image capture, processing and integration with wireline log data.

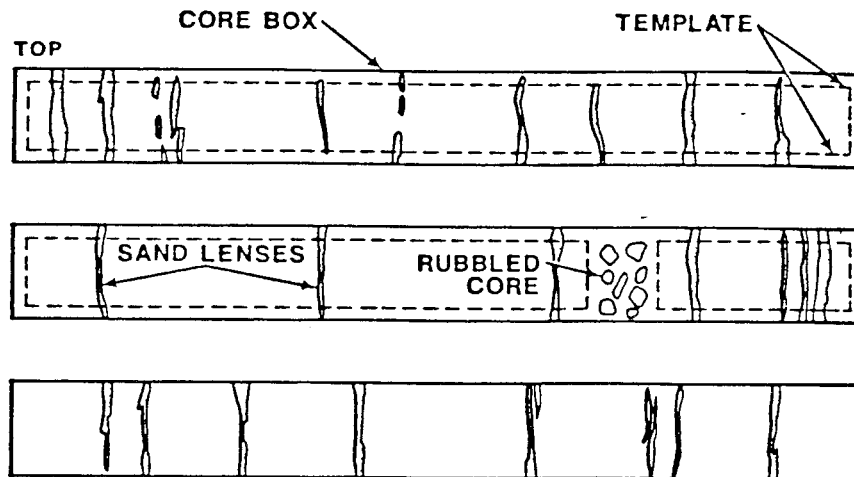


Figure 2. Sketch of UV-core photographs with typical thin sand lenses. Also depicted are the user-defined templates for eliminating unwanted artifacts (i.e., core box edges or rubble core) from the image analysis.

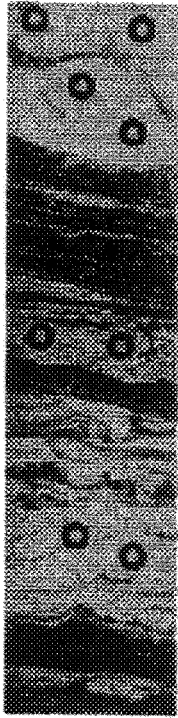


Figure 3a - Selected pixels used in the training set.

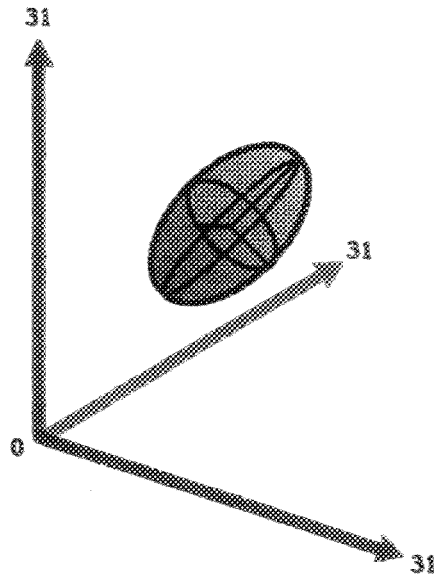


Figure 3b - The Elliptical Cloud calculated from the training set.

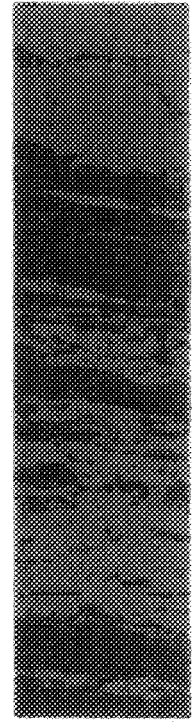


Figure 3c - Processed image with green representing colors within ellipsoid.

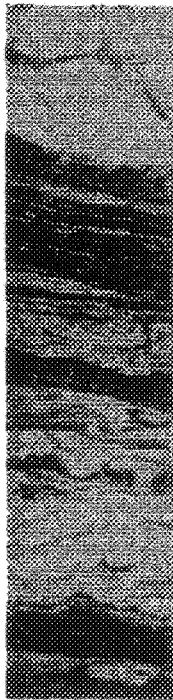
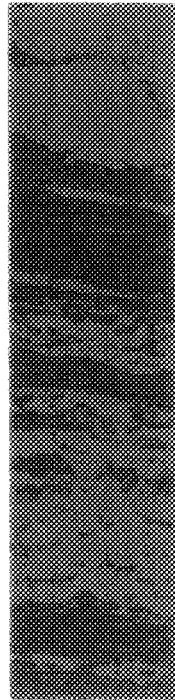
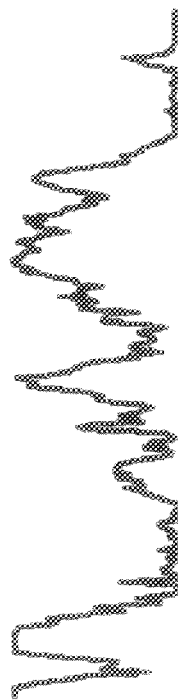


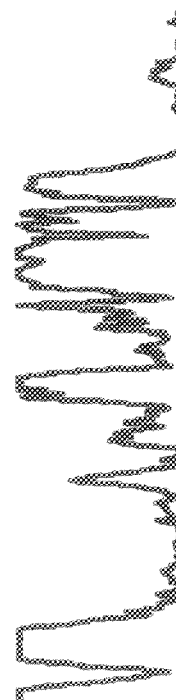
Figure 3d - UV Light



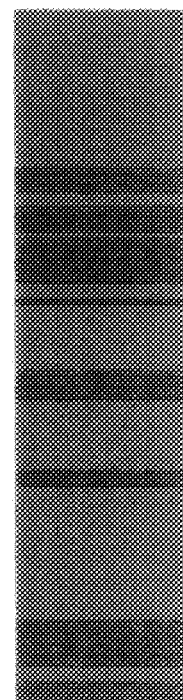
Processed Binary Image





Sand-Shale Ratio (Zero Degree Dip)



Sand-Shale Ratio (Ten Degree Dip)



Binary Sand Flag (Based on 50% Sand-Shale Ratio Threshold)
 Sand  Shale

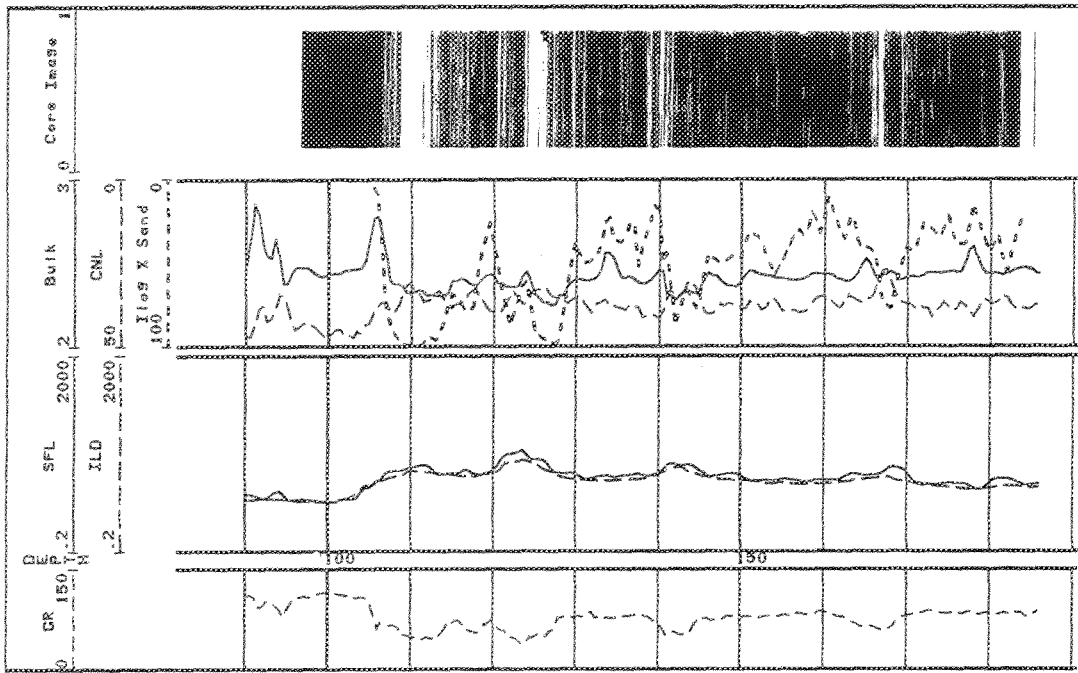


Figure 5. Core image with conventional log data from an Alaskan laminated sand sequence.

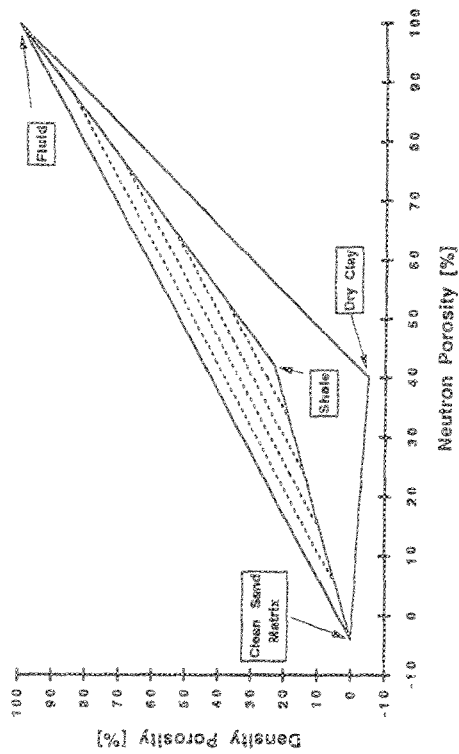


Figure 4. Generalized, pseudo-mineral triangles for determination of porosity, V_{ss} and V_{sh} from neutron and density log data.

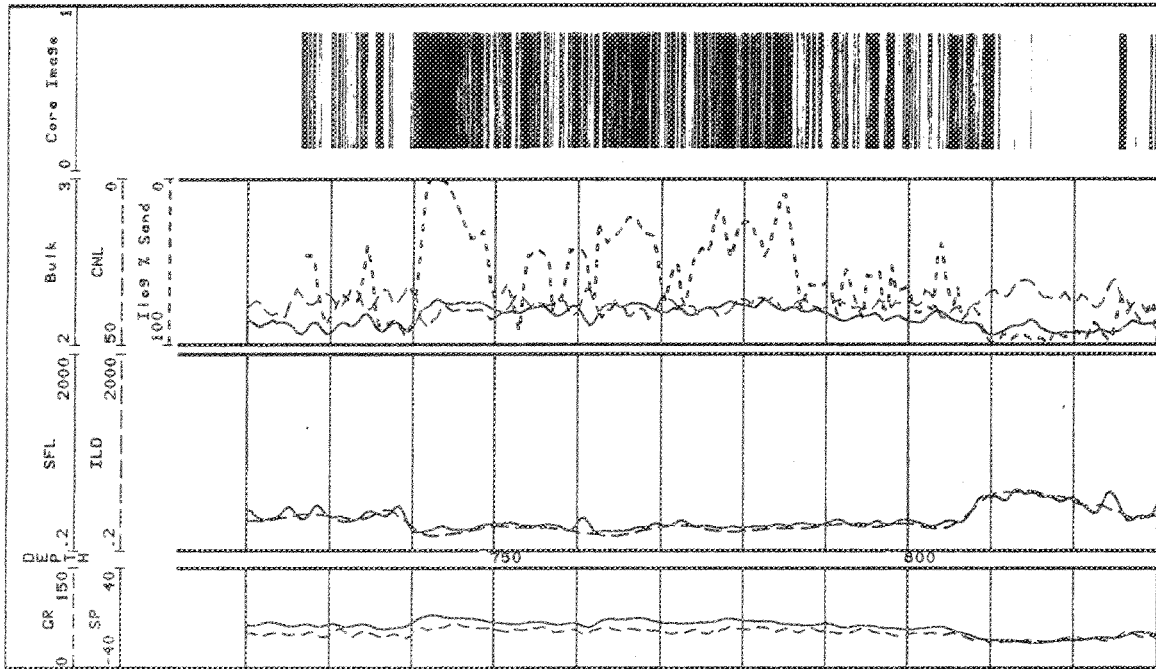


Figure 6. Core image with conventional log data from a Gulf Coast laminated sand sequence.

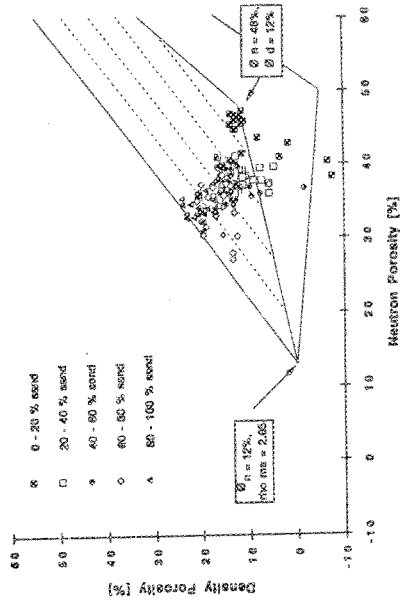


Figure 7a. Neutron-density crossplot for Vsh determination for the Alaskan example.

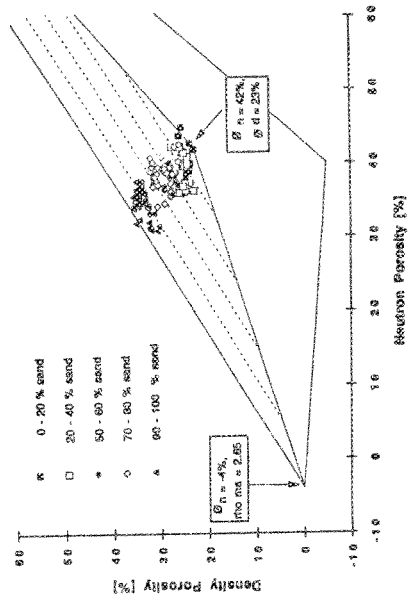


Figure 7b. Neutron-density crossplot for Vsh determination for the Gulf Coast example.

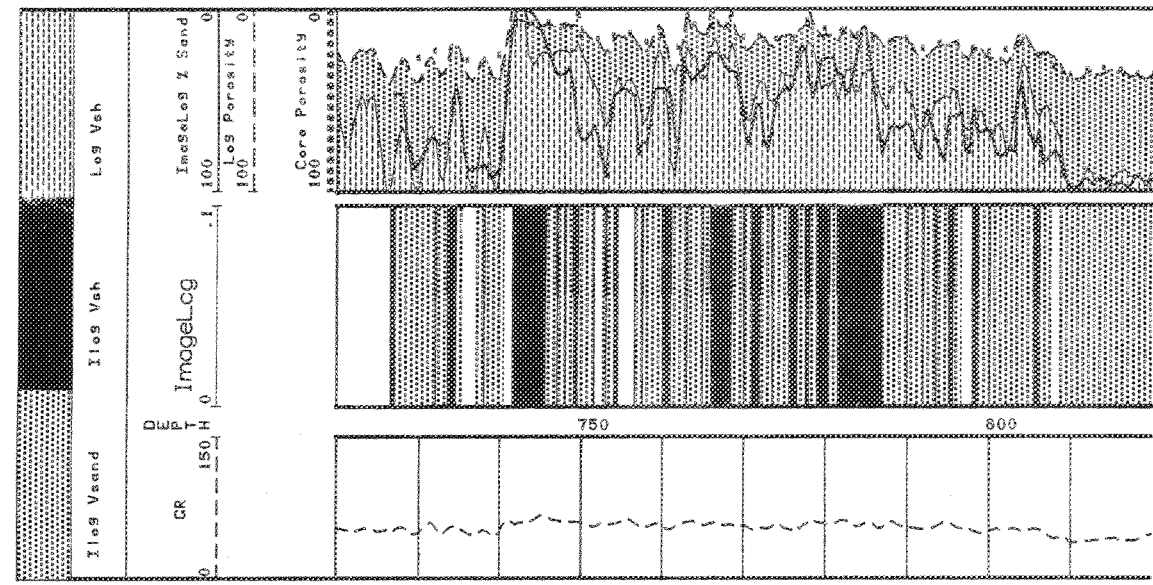


Figure 8a. Core image data with log computed Vsh. The image analysis percent sand nearly equals the compliment of Vsh for the Alaskan laminated sand example.

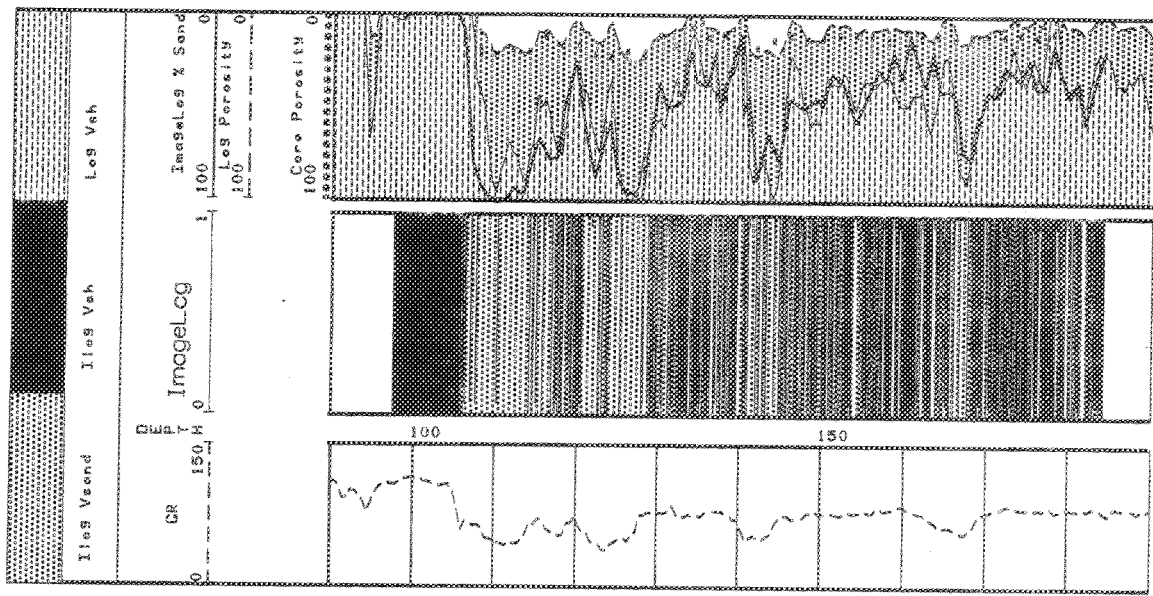


Figure 8b. Core image data with log computed Vsh. The image analysis percent sand nearly equals the compliment of Vsh for the Gulf Coast example.

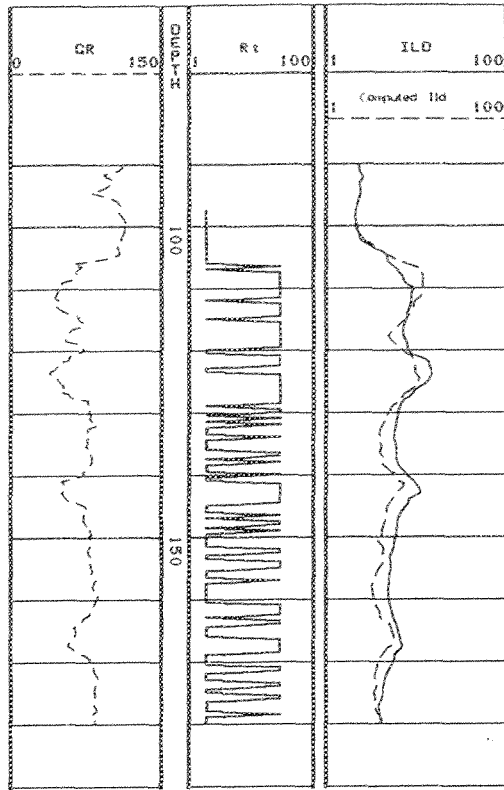


Figure 9a. Initial Rt and Ild vs Computed Ild

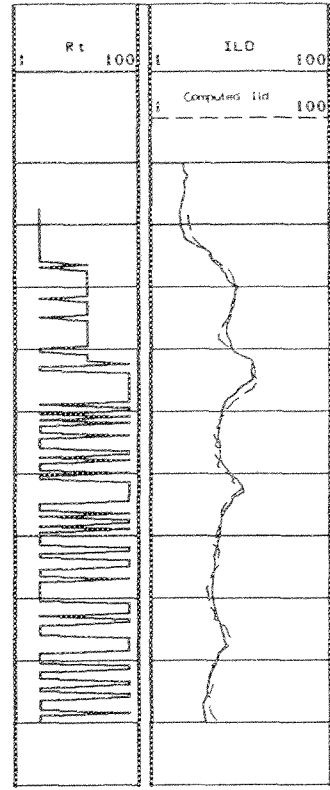


Figure 9b. Final Rt with Computed Ild = Ild

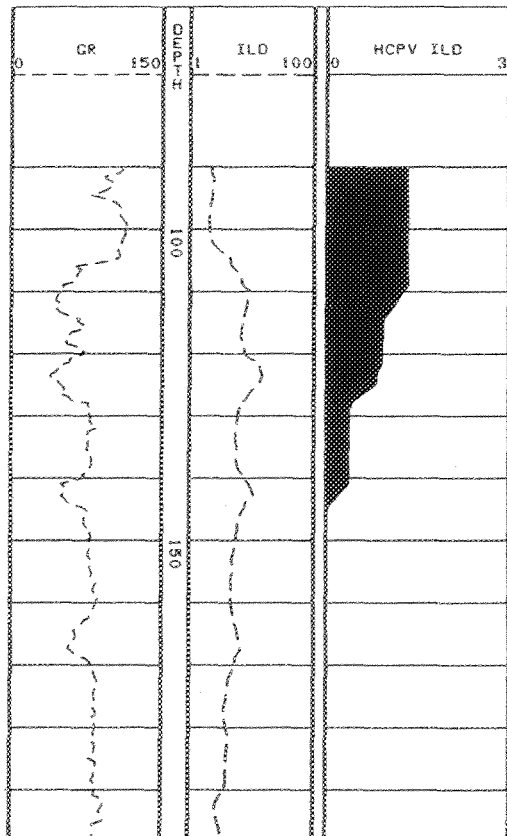


Figure 10a. Initial HCPV using Ild for Rt

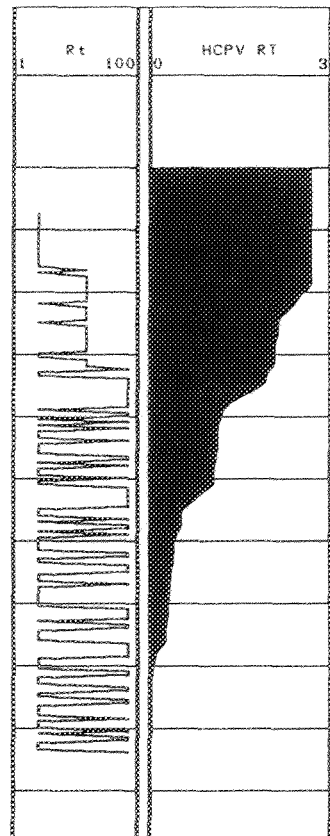


Figure 10b. Final HCPV with Rt from forward modeling